Article

Aerodynamic Characteristics of Airfoil and Vertical Axis Wind Turbine Employed with Gurney Flaps

Yosra Chakroun † and Galih Bangga †,*

Institute of Aerodynamics and Gas Dynamics, University of Stuttgart, Pfaffenwaldring 21, 70569 Stuttgart, Germany

* Correspondence: bangga@iag.uni-stuttgart.de
† These authors contributed equally to this work.

Abstract: In the present studies, the effects of Gurney flaps on aerodynamic characteristics of a static airfoil and a rotating vertical axis wind turbine are investigated by means of numerical approaches. First, mesh and time step studies are conducted and the results are validated with experimental data in good agreement. The numerical solutions demonstrate that the usage of Gurney flap increases the airfoil lift coefficient C_L with a slight increase in drag coefficient C_D. Furthermore, mounting a Gurney flap at the trailing edge of the blade increases the power production of the turbine considerably. Increasing the Gurney flap height further increases the power production. The best performance found is obtained for the maximum height used in this study at 6% relative to the chord. This is in contrast to the static airfoil case, which shows no further improvement for a flap height greater than 0.5%c. Increasing the angle of the flap decreases the power production of the turbine slightly but the load fluctuations could be reduced for the small value of the flap height. The present paper demonstrates that the Gurney flap height for high solidity turbines is allowed to be larger than the classical limit of around 2% for lower solidity turbines.

Keywords: aerodynamics; CFD; flow characteristics; gurney flap; wind energy

1. Introduction

Wind energy plays an important role in providing clean renewable energy for society. It is sustainable and has a smaller impact on the environment when compared with the energy from fossil fuels [1]. Many types of wind turbines have been invented as a result of long-term research and development. According to the axis of rotation, wind turbines can be mainly classified into horizontal axis wind turbines (HAWTs) and vertical axis wind turbines (VAWTs). Due to the increased interest in employing wind turbines also in built environments, the popularity of VAWTs has increased considerably. There are several advantages to VAWT, such as its independence from wind direction and its ability to withstand high turbulence.

VAWTs are currently always under development and investigation for their construction, structures, as well as aerodynamic property optimization. The fact that VAWTs experience dynamic stall at its blades is challenging blade engineers to improve the performance and its self-starting ability [2–5]. Dynamic stall is a common phenomenon that appears mainly on the rotating rotor blades, and it becomes one of the most limiting factors in aerodynamic performance [6]. It is also likely unpreventable during the operation of VAWTs in low tip speed ($\lambda \leq 3$) [5]. In order to verify this common event, many studies have been carried out through various experiments using computational simulations. An experiments by McCroskey et al. [6] using a model rotor and an experiment by Martin et al. [7] using flow visualization techniques confirm the presence of dynamic stall as the result of a vortex-dominated flow field. In order to predict dynamic stall development especially on a VAWT, simulations using different turbulence models and different numerical techniques are executed by Ferreira et al. [4] and by Almohammadi et al. [8]. Regardless

of the methods or the types of studies, it needs to be underlined that dynamic stall has a strong influence on the loads and the forces at the rotor blades.

One possible way to control the low aerodynamic performance of VAWT is by using flow control devices. Studies on flow control devices on wind turbine performance in terms of loads and noise emission have been conducted in the past. One example of such flow control technologies is a Gurney flap (GF). This device is located at the trailing edge of the airfoil blade with the goal of enhancing its lift coefficient. As a result, this will increase the positive camber and induce counterrotating vortices downstream of the airfoil, which has a significant flow turning over in the vicinity of the flap region [9]. This decreases the momentum deficit in the wake and generates an increased lift effect. GF has been commonly applied for HAWTs and has proven to be beneficial for increasing power production [10,11]. This step has been followed by several investigations for VAWTs [12–14]. Zhu et al. [14], for example, evaluated the effects of rotor solidity (0.175–0.5) on the turbine performance employed with Gurney flaps. They found that the load fluctuations decrease when the solidity of the turbine increases, followed by the performance reduction. However, this study was performed by artificially increasing the blade number up to 5 to increase the rotor solidity. The conclusions could be different for a two-/three-bladed rotor having the same rotor solidity. Yan et al. [15] investigated the aerodynamic performance of a VAWT employed with gurney flaps. The studies demonstrated that the performance of the rotor increases in the low tip-speed regime while it decreases at a higher rotational speed. These studies were limited to two values of Gurney flap heights. Syawitri et al. [12] also evaluated Gurney flap effects on VAWTs, but the investigations were only focused on integrated loads. Very recently, Zhu et al. [13] assessed the Gurney flap height on VAWT power production. The results are consistent with that of other studies. They further demonstrated that severe aerodynamic loss can occur when the Gurney flap heights were 1.5% and 1.75% of the chord length. Despite this fact, their studies were based on a turbine operating at a large rotational speed having a relatively low solidity. The results might not be generalizable for a larger solidity turbine. In fact, high solidity turbines equipped with Gurney flaps are rarely investigated in existing literature.

From the above discussion, one can see that the main effects of Gurney flaps on azimuthal loads and flow characteristics are far from being fully understood and optimized. This is especially true since VAWTs generally operate at a constant variation in the angle of attack and often under harsh environment. Furthermore, the blade rotation complicates the effects and the blade operates in the wake within half of its cycle in the downwind regime. Thus, the conclusions obtained from one study are often not generalizable. Therefore, the present studies intend to investigate the effect of Gurney flaps mounted on VAWTs for improving the understanding towards this issue and to explore the physical flow interactions and characteristics.

The main goal of the paper is to assess Gurney flap effects on loads acting on wind turbine blades. To do so, the studies will be divided into two aspects: (1) non-rotating and (2) rotating situations. The earlier and the latter approaches will be needed to differentiate the effects. This will be important because VAWT usually works under harsh conditions where the angle of attack changes continuously during operation from positive to negative values. In this part of the studies, the evaluations are focused on the aerodynamic forces of the airfoil by varying the Gurney flap parameters. Second, the studies are then extended by applying the Gurney flap on a rotating two-bladed vertical axis wind turbine. In this part of the studies, the assessments are focused on rotor performance in terms of the integral and azimuthal loads. The flow field surrounding the blade and the source of power improvement will be discussed and evaluated.

2. Flow Solver FLOWer

The present studies were conducted employing a computational fluid dynamics (CFD) code FLOWer. The basic version of the CFD code FLOWer was developed by the German Aerospace Center (DLR) within the MEGAFLOW project [16] in the late 1990s. It is a

compressible code and solves the three-dimensional Navier–Stokes equations in an integral form with several turbulence models available. The code has been extended significantly at the Institute of Aerodynamics and Gas Dynamics (IAG) in the last decade. The numerical scheme is based on a finite-volume formulation for block-structured grids. The spatial discretization scheme used in the present study is a central cell-centered Jameson–Schmidt–Turkel (JST) [17] finite volume formulation because it provides high robustness and is well-suited for parallel applications. This numerical method provides a second-order accuracy in space. This is done by utilizing a central space discretization with an artificial viscosity. An explicit hybrid 5-stage Runge–Kutta time-stepping scheme was applied. For complex cases, FLOWer supports an overlapping chimera (overset) approach [18–20]. This allows each mesh component to be generated separately while maintaining its quality. For solving the time-dependent case, dual time-stepping [21] and the multi-grid approach with an implicit residual smoothing and variable coefficients [22] were applied. Using the ROT module, one could simulate body motions in the rotating frame of reference needed for unsteady wind turbine simulations. The code is fully optimized for parallel computations using a Message-Passing Interface (MPI). For turbulence closure, and the unsteady Reynolds-Averaged Navier–Stokes (URANS) approach employing the shear stress transport (SST) $k - \omega$ model [23] was used in the present work because the model is accurate for flows with a strong adverse pressure gradient. The mathematical formulations of the model are as follows:

$$\frac{\partial \rho k}{\partial t} + \frac{\partial \rho u_j k}{\partial x_j} = P - \beta^* \rho \omega k + \frac{\partial}{\partial x_j}\left[(\mu + \sigma_k \mu_t)\frac{\partial k}{\partial x_j}\right] \tag{1}$$

$$\frac{\partial \rho \omega}{\partial t} + \frac{\partial \rho u_j \omega}{\partial x_j} = \frac{\gamma \omega}{\nu_t} P - \beta \rho \omega^2 + \frac{\partial}{\partial x_j}\left[(\mu + \sigma_\omega \mu_t)\frac{\partial \omega}{\partial x_j}\right] + 2(1 - F_1)\frac{\rho \sigma_{\omega 2}}{\omega}\frac{\partial k}{\partial x_j}\frac{\partial \omega}{\partial x_j}. \tag{2}$$

The parameters used in these equations are determined as

$$P = \tau_{ij}\frac{u_i}{x_j} \tag{3}$$

$$\tau_{ij} = \mu_t\left(2S_{ij} - \frac{2}{3}\rho\, k\, \delta_{ij}\right) \tag{4}$$

$$S_{ij} = \frac{1}{2}\left(\frac{u_i}{x_j} + \frac{u_j}{x_i}\right) \tag{5}$$

$$\mu_t = \frac{\rho\, a_1\, k}{\max(a_1\, \omega, \Omega\, F_2)}. \tag{6}$$

3. Static Airfoil Case

In this section, the analyses carried out for a static airfoil employed with a Gurney flap at various configurations are ddetailed. The studies were conducted for the NACA 4412 airfoil, having a relative thickness of about 12%. The Reynolds number was around 1.86 million. Indeed, this value is a little small for modern HAWTs, but VAWTs generally operate at very small rotational speeds. Thus, their Reynolds numbers are also smaller. First, the impacts of spatial and temporal discretizations on the resulting aerodynamic loading under static conditions were investigated on the clean airfoil without the Gurney flap. Having obtained a suitable numerical setup, quantitative and qualitative computational data on the performance of the gurney flap on the airfoil were carried out. Computations of the airfoil equipped with a gurney flap were compared with experimental data in order to determine the effect of Gurney flap parameters on the lift and the drag coefficients.

3.1. Mesh Configurations

In order to discretize the airfoil in space, the O-mesh topology was employed since it offers a high resolution of the flow in the boundary layer and avoids unnecessary

cells downstream of the profile. The two-dimensional (2D) mesh was created using an automated script developed at the institute in a grid generator Pointwise. The farfield was located at 150 times the chord length. A large farfield distance was set to prevent the farfield domain from reflecting flow. The high-quality meshes for airfoil and Gurney flap were created independently and combined using the chimera approach. The boundary layer was fully resolved with a non-dimensional y^+ near the wall less than unity. Thirty-two-cell layers were located within the boundary layer regime with a growth rate of 1.1. The boundary conditions were set in the mesh as well as around it as shown in Figure 1.
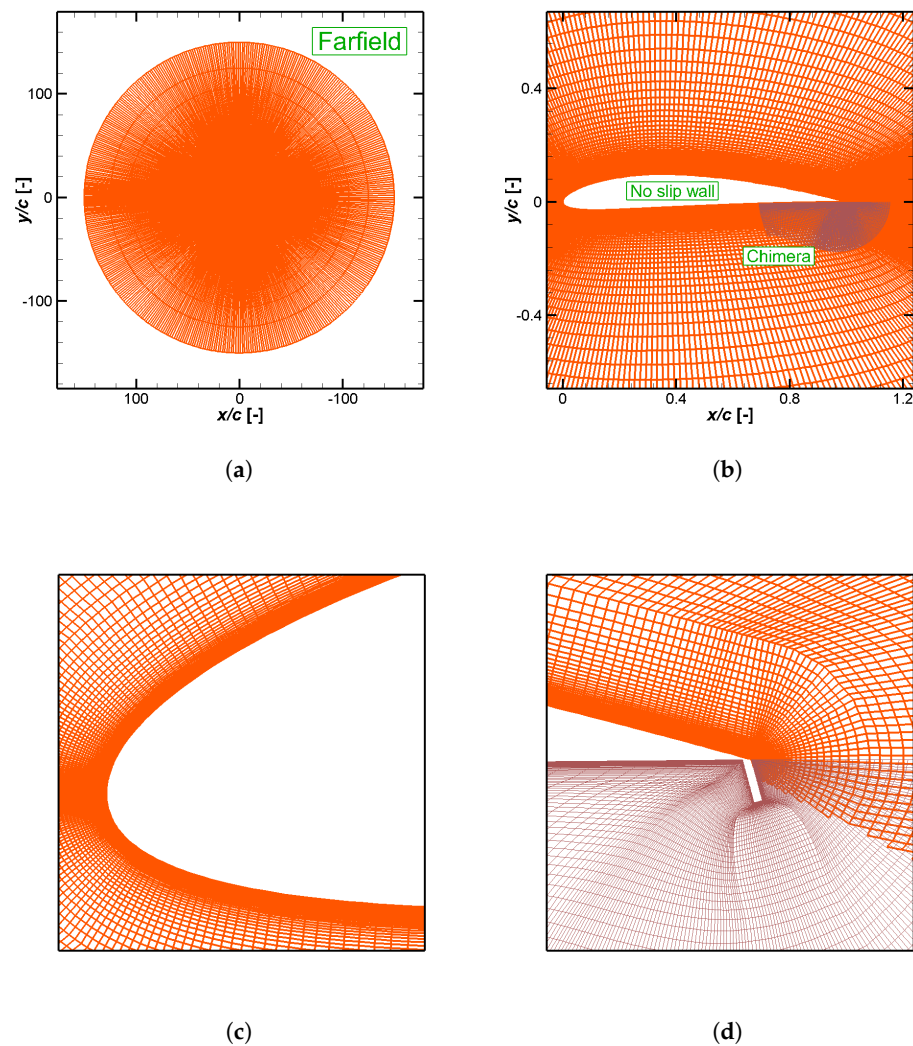

Figure 1. Computational mesh of the static airfoil and applied boundary conditions. (**a**) Overall mesh, (**b**) enlarged views near the airfoil (**c**) near the leading edge and (**d**) near the trailing edge.

The farfield boundary condition was used for the outer side of the domain, and a non-slip boundary condition was applied around the airfoil with the purpose of simulating the viscous wall of the airfoil assuming a zero flow velocity. In the following sections, time step studies as well as grid studies were performed to keep the computational costs low while still retaining reasonable accuracy of the flow solutions.

3.2. Influence of the Grid Refinement

For the spatial discretization study, the grid along the baseline was refined from 71,680 cells to 97,280 cells. A coarser grid 51,200 cells of cells was also tested. According to the grid convergence index introduced by Celik et al. [24], the grid refinement should be at

least by a factor of 1.4. The simulations for the grid studies were performed using the time step size $\Delta t = t_c/75$ (with t_c being the convective time of the fluid flow over the airfoil, i.e., c/U_∞) at a Reynolds number of 1.86×10^6. Detail is given in Table 1.

Table 1. Spatial discretization data for the clean static NACA 4412 airfoil.

Grid Name	Circumferential	y^+	BL Layers	Number of Cells
G1	290	<1.0	32	51,200
G2	416	<1.0	32	71,680
G3	576	<1.0	32	97,280

Figure 2a presents the variation in the lift coefficient C_L versus the angle of attack α. The computed lift coefficient C_L of the NACA 4412 airfoil from the simulation for the three different grid resolutions as well as the lift coefficient from the experimental data and CFD reference data are compared. Figure 2b shows the variation in the lift coefficient versus the drag coefficient for the simulated CFD data in comparison with the experimental data. The refinement has a very small impact on the increase in the lift coefficient. Generally, finer grid and time resolutions produce more accurate results than coarser ones, but it is followed by an increase in the computational expenses as a consequence. Therefore, it is reasonable to use a medium grid resolution (71,680 cells) and the time step size $\Delta t = t_c/75$ for subsequent simulations. It is noted that, in the present comparison, the predicted forces are already independent from the number of cells from the coarsest grid resolution G1. In fact, it has been documented in previous works [25–27] that this amount of grid cells was sufficient for load predictions. The results from the present work further confirm these past studies.
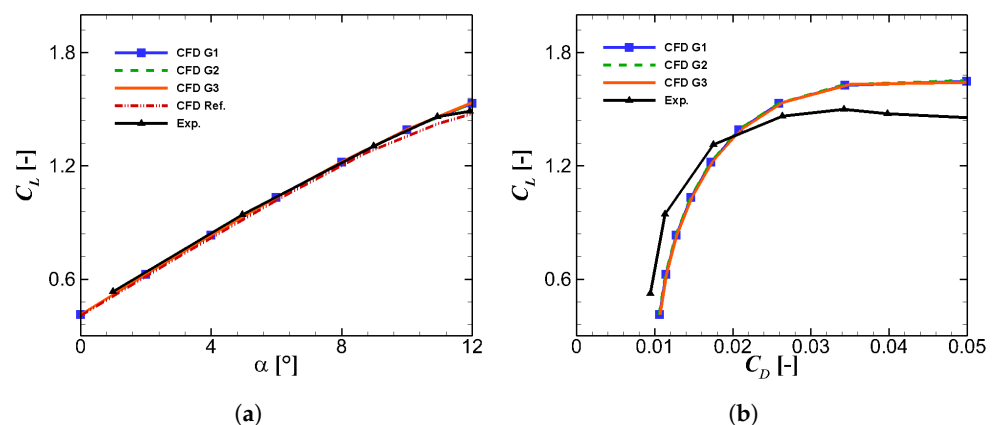

(a)   (b)

Figure 2. Comparison of computational fluid dynamics (CFD) simulations executed for three different grid resolutions (G1: 51.200 cells, G2: 71.680 cells, and G3: 97.280 cells) to an experimental [28] and a reference CFD data [29] for the clean airfoil. (**a**) Lift and (**b**) drag.

3.3. Influence of the Gurney Flap Grid Refinement

Thus far, the computational setup for the baseline is validated, and the time step as well as the grid resolution are chosen (G2: 71,680 cells and $\Delta t = t_c/75$). In this section, the objective is to provide quantitative data on the performance of a Gurney flap. For the spatial discretization study of the Gurney flap mesh, the grid along the Gurney flap was refined from 17,920 cells to 32,000 cells. A coarser grid of 8960 cells was also tested for comparison. Detail is given in Table 2.

Table 2. Grid parameters of the Gurney flap applied on the NACA 4412 airfoil.

Grid Name	y^+	Number of Cells
GF1	<1.0	8,960
GF2	<1.0	17,920
GF3	<1.0	32,000

Figure 3a presents the variation lift coefficient C_L versus the angle of attack α. The computed lift coefficient C_L of the GF from the simulation for the three different grid resolutions as well as the lift coefficient from the experimental data and CFD reference data are compared. Figure 3b shows the variation in the lift coefficient versus the drag coefficient for the simulated CFD data in comparison with the experimental data. One can see that the grid independence state has been reached for this case. Increasing the number of the grid cells will not improve the prediction accuracy; instead, it only increases the computational cost. Lift and drag are able to be predicted fairly accurately, even better than the reference CFD data from [29]. Therefore, the medium grid resolution (G2) can be used for subsequent evaluations.
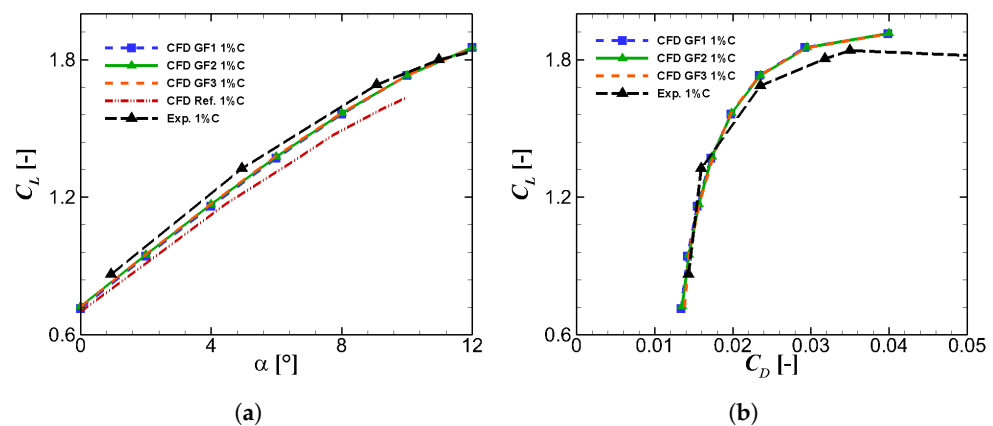

Figure 3. Comparison of CFD simulations executed for three different grid resolutions to an experimental [28] and a reference CFD data [29] for the static airfoil equipped with a Gurney flap with height $h = 1\%c$. (**a**) Lift and (**b**) drag.

3.4. Comparison with Experimental Data

Now that a suitable CFD setup has been found, CFD computations are then compared to the experimental data and CFD reference data for different Gurney flap configurations. Therefore, the NACA 4412 airfoil is equipped with a Gurney flap with a flap angle of 90° for three different flap heights, namely, 0.5%c, 1.5%c, and 2%c.

Figure 4a presents the lift coefficient (C_L) curve at different angles of attack in comparison with the measured data. The angle of attack varies between 0° and 12°. It can be seen that the CFD computations for the GF height of 0.5% are able to model the behavior of the lift coefficient fairly well, better than the reference CFD data. Figure 4b shows the lift coefficient C_L over the drag coefficient (C_D). The CFD simulations deliver good prediction of the lift-to-drag characteristics.
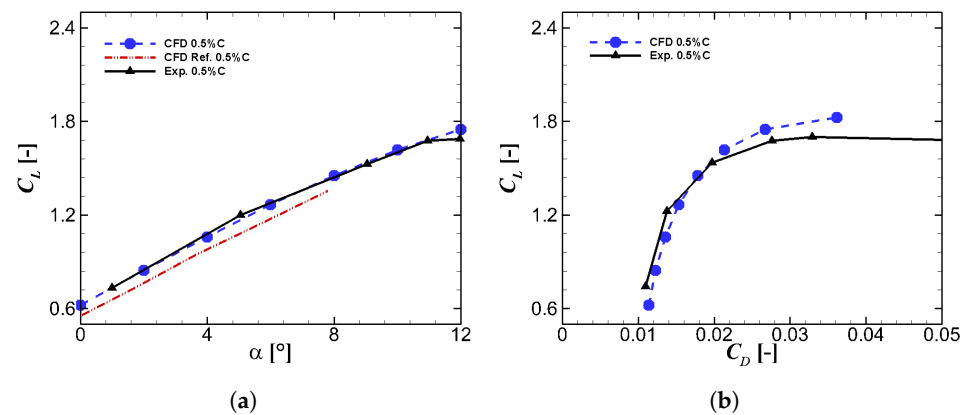
Figure 4. Comparison of CFD simulations executed on the static airfoil equipped with a Gurney flap at the trailing edge for a Gurney flap height of 0.5%c and a Gurney flap (GF) angle of 90° to the reference data [28,29]. (**a**) Lift and (**b**) drag.

By increasing the Gurney flap height from 0.5%c to 1.5%c and 2.0%c , one can see that the prediction accuracy is not heavily affected. The main characteristics of the lift and drag polar are still able to be reconstructed in the present CFD simulations, as shown in Figures 5 and 6 for the GF heights 1.5% and 2%, respectively, which further increase the confidence about the accuracy of the employed CFD setup in the present work.
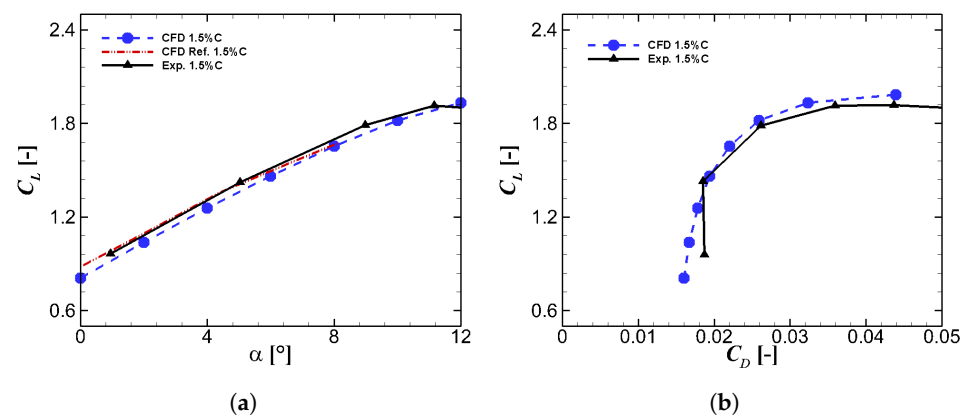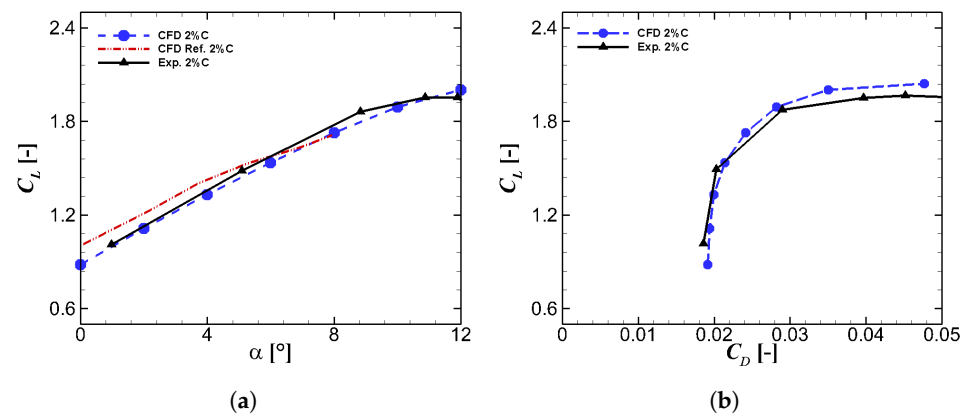

Figure 5. Comparison of CFD simulations executed on the static airfoil equipped with a Gurney flap at the trailing edge for a Gurney flap height of 1.5%c and a GF angle of 90° to the reference data [28,29]. (**a**) Lift and (**b**) drag.

Figure 6. Comparison of CFD simulations executed on the static airfoil equipped with a Gurney flap at the trailing edge for a Gurney flap height of 2.0%*c* and a GF angle of 90° to the reference data [28,29]. (**a**) Lift and (**b**) drag.

3.5. Influence of the Gurney Flap Height

Figure 7a demonstrates how the lift force increases with increasing Gurney flap height. As an example, a 2%*c* Gurney flap shifts the $C_L - \alpha$ curve by more than 4° in comparison with the clean airfoil case. The effect on C_D using various Gurney flap heights can be seen in Figure 7b. The addition of the Gurney flap increases C_D considerably. However, the flap height of 0.5%*c* results in va ery small increase in drag at low angles of attack. Figure 7c presents the result of the lift-to-drag ratio vs. the angle of attack. Large drag penalties due to the usage of a Gurney flap can be observed at low-to-moderate angles of attack ($0° < \alpha < 8°$), which can be decreased by reducing the flap height. However, at higher angles of attack ($\alpha > 8°$), lift and drag are both enhanced. As a consequence, Gurney flap has a minimal effect on C_L/C_D. It is shown that a 0.5%*c* GF provides an increased lift-to-drag ratio for the whole range of angles of attack considered in the studies. Liebeck et al. [30] and Li et al. [31] suggested that C_D could increase when the height of the Gurney flap is greater than 2%*c*. Giguere et al. [29] inferred that the optimal Gurney flap size depends on the flow field at the trailing edge of the airfoil.
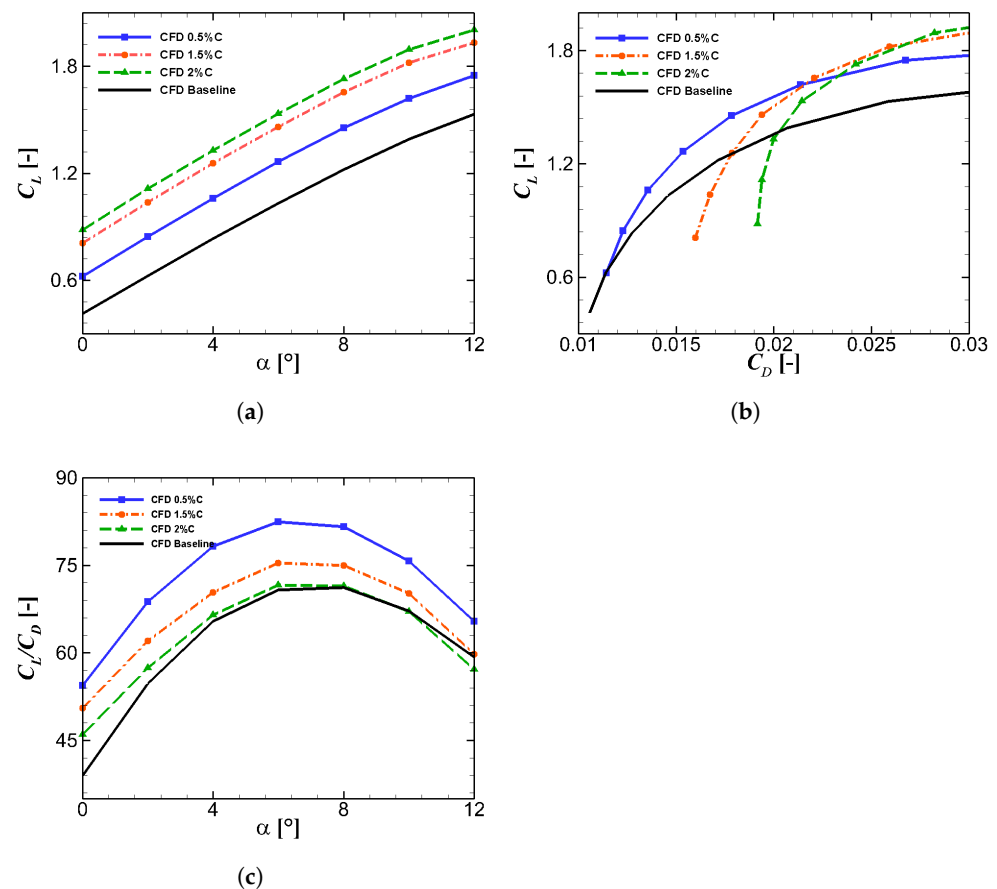
(a)

(b)

(c)

Figure 7. Gurney flap height effect on the aerodynamic performance of the NACA 4412 airfoil for a GF angle of 90°. (**a**) Lift, (**b**) drag and (**c**) aerodynamic efficiency.

3.6. Influence of the Gurney Flap Angle

The characteristics of the lift coefficient as a function of the flap angle are presented in Figure 8a. It can be seen that both studied flap angles (90° and 105°) increase the C_L levels compared with the baseline airfoil case, but the improvement is slightly greater for the 90° angle. Figure 8b shows that there is a drag penalty by applying the Gurney flap at the trailing edge of the airfoil. This effect can be reduced by increasing the flap angle. Comparable results are also obtained by mounting the Gurney flap at the 90° and 105° angles for the 2%c height presented in Figure 9.
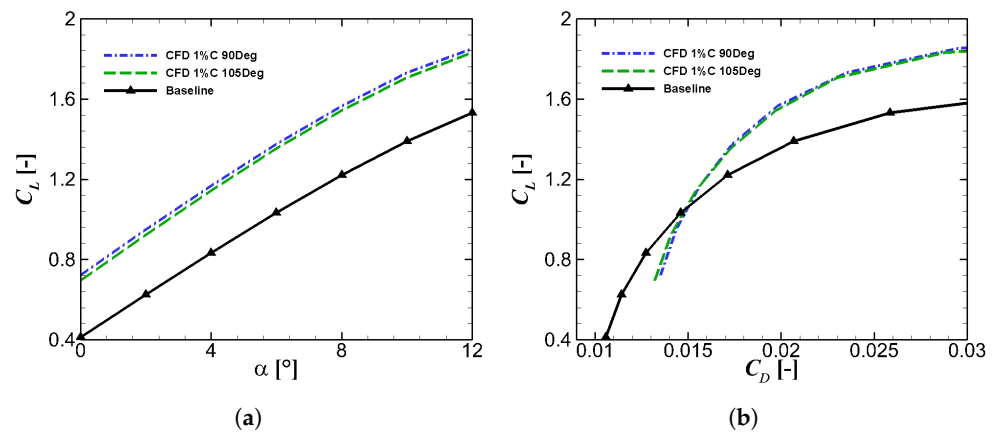
Figure 8. Effect of the Gurney flap angle on the aerodynamic performance of the NACA 4412 airfoil for a GF height of 1%*c*. (**a**) Lift and (**b**) drag.
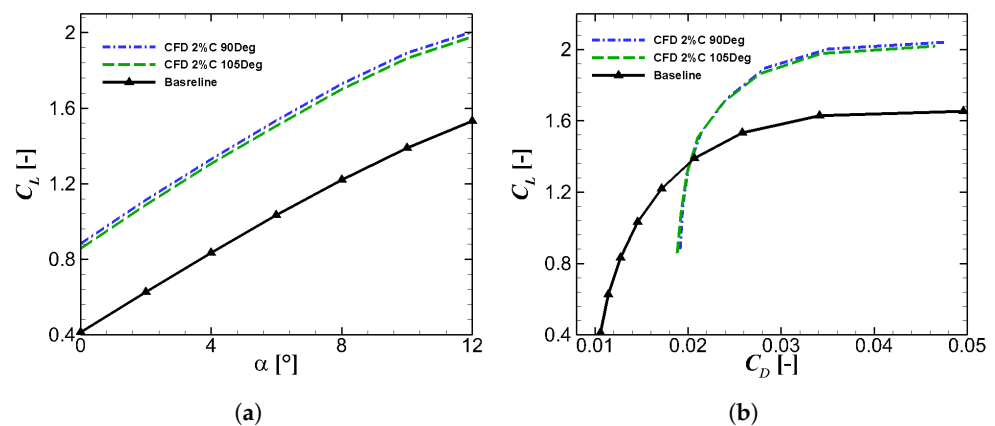
Figure 9. Effect of the Gurney flap angle on the aerodynamic performance of the NACA 4412 airfoil for a GF height of 2%*c*. (**a**) Lift and (**b**) drag.

4. Rotating VAWT Case

In this section, the employed vertical axis wind turbine is described, including its coordinate system. Then, the scenario and strategy for mesh studies are described in detail. Lastly, the simulation results is presented in the last section and discussed considering the dynamic stall phenomena on the performance of the VAWT.

4.1. The Studied Turbine and Operating Conditions

Computational fluid dynamics (CFD) studies were performed on a straight-two-bladed vertical axis wind turbine. The turbine operated at a wind speed of 8 m/s. Measurements [32] of this turbine were conducted for tip speed ratios ranging from $\lambda = 0.50$ to $\lambda = 3.0$. The investigated turbine had a rotor radius of 1 m, a pitch angle of 6°, and a chord length of 0.265 m. This turbine employed a NACA 0021 airfoil having a rotor solidity ($\sigma = Nc/R$) of 0.53. The characteristics of the investigated turbine are also listed in Table 3. The coordinate system (CS) and the force acting on the turbine are defined in Figure 10.

Table 3. Characteristics of the investigated vertical axis wind turbine.

Parameters	
Type	H-Darrieus
Airfoil	NACA-0021
Solidity(σ)	0.53
Number of blades	2
Radius(R)	1.0 m
Pitch angle (α_p)	6°
Chord length (c)	0.265 m
Operating range	$0.5 < \lambda < 3.0$
U_∞	8 m/s
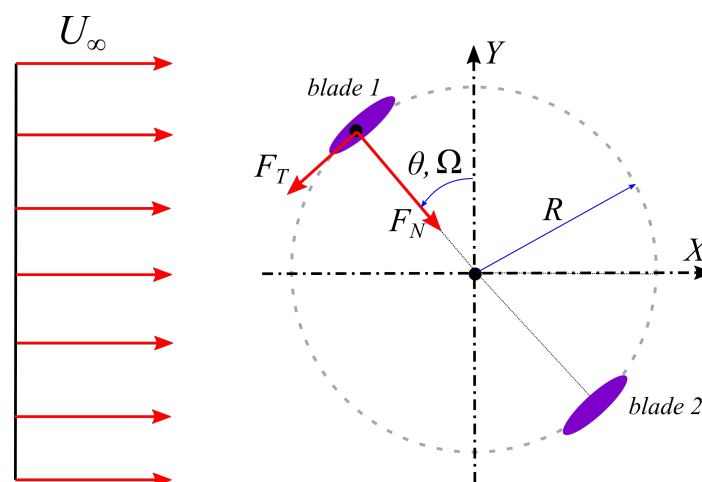
Figure 10. The employed coordinate system in the study.

4.2. Mesh Configuration

The structured mesh technique was employed in the present work. The mesh structures consist of four components: background, wake refinement, rotor, and Gurney flap meshes, as depicted in Figure 11. Similar to the static airfoil case, the overlapping grid (chimera) technique was applied in the studies. This allows one to generate high-quality meshes separately for each component of the grid. This is helpful for simplifying the mesh generation process. In the present work, the background mesh has 329×193 grid points, respectively, in the X and Y directions. The size of the domain is $-25R \times 120R$ in X and $50R$ in Y. The mesh is refined significantly near the rotor location. In this area, the mesh has a cell size of $\Delta/D \approx 0.12$ ranging from $X = -5R$ to $25R$. This particular grid has 257×141 points, respectively, in the X and Y directions. Past studies have shown that the employed mesh is already sufficient for accurately modelling the aerodynamic characteristics of this turbine and that the solutions are grid independent [2]. This conclusion also applies for the wake resolution; as such, the wake refinement mesh was increased up to 513×201 grid points ($\Delta/D \approx 0.06$) [2].
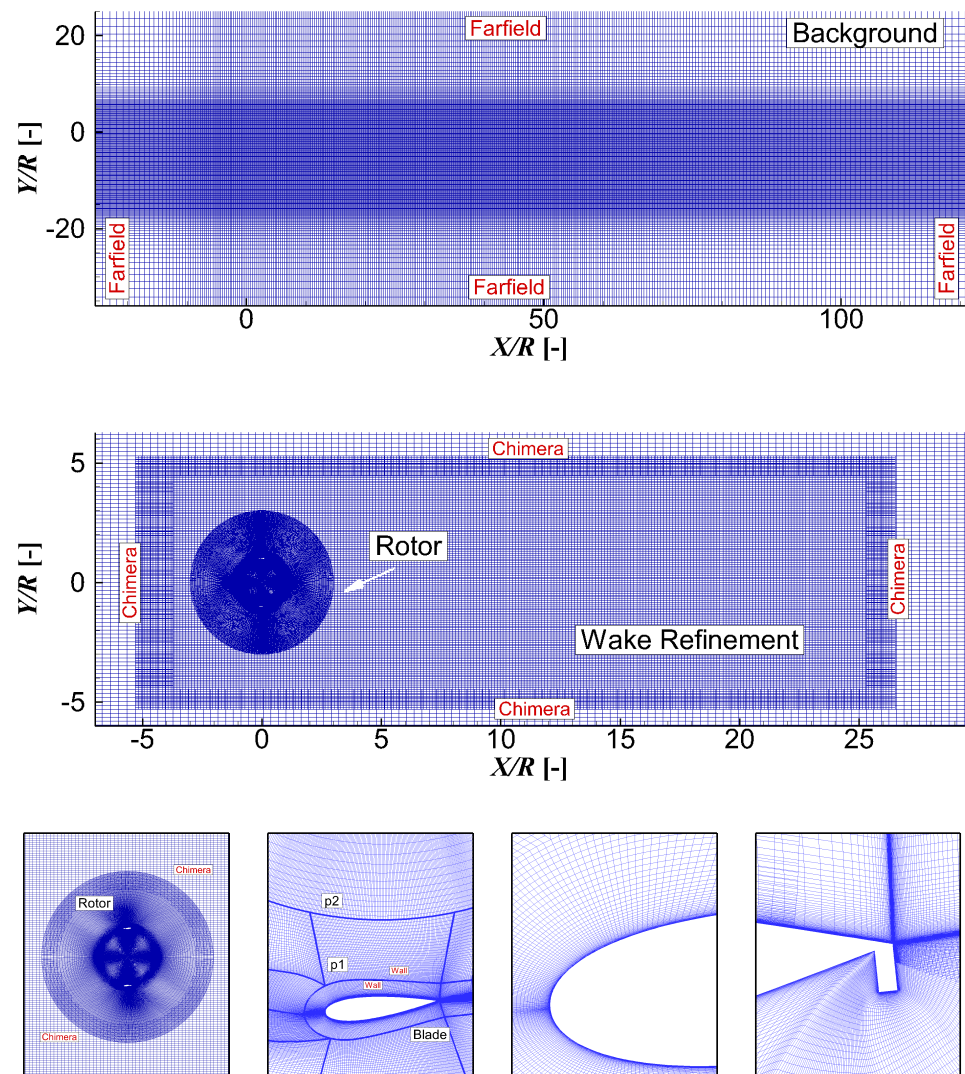
Figure 11. Mesh assembly for vertical axis wind turbine (VAWT) computations consisting of the background mesh, wake refinement mesh, rotor mesh, and Gurney flap mesh.

4.3. Comparison with Experimental Data

In this section, the accuracy of the CFD computations is quantified by comparing the results with experimental data [32] and IDMS (Improved Double-Multiple-Streamtube) calculation in terms of the integrated and azimuthal loads for the baseline case without the Gurney flap. The IDMS method is described in detail in [33]. The power generated by the wind turbine and the tip speed ratio are defined as follows:

$$C_{Power} = \frac{P_{Turbine}}{\frac{1}{2}\rho U_\infty^3 2R} \tag{7}$$

$$\lambda = \frac{\Omega R}{U_\infty} \tag{8}$$

with $P_{Turbine}$, ρ, Ω, U_∞, and R being power, air density, rotational speed, wind speed, and rotor radius, respectively. The azimuthal loads are defined as follows:

$$C_n = \frac{F_n}{\frac{1}{2}\rho U_\infty^2 2R} \tag{9}$$

$$C_t = \frac{F_t}{\frac{1}{2}\rho U_\infty^2 2R} \tag{10}$$

where F_n and F_t are, respectively, the sectional normal and tangential forces.

Figure 12 shows the the predicted power curve using CFD for three different time step sizes in comparison with the measurement data [32]. The time step size is defined based on the period of the turbine rotation (T). One can see that refining the time step size improves the prediction accuracy of the CFD solutions. The best prediction accuracy is obtained for the finest time step size of $T/1440$, although the change between this time step with the coarser one ($T/720$) is not significant. For all subsequent investigations, the time step size of $T/1440$ will be used. To obtain a deeper insights into the prediction results over the azimuth, the normal and tangential forces of the blade are presented in Figure 13. Here, it can be observed that good agreement is also obtained for the azimuthal loads. Some deviations are observed at the azimuth angles close to zero and larger than 270° for the normal loads component. For the tangential component, the downwind part is very difficult to be predicted because it is associated with separated flow and the tangential force is highly influenced by the drag component.
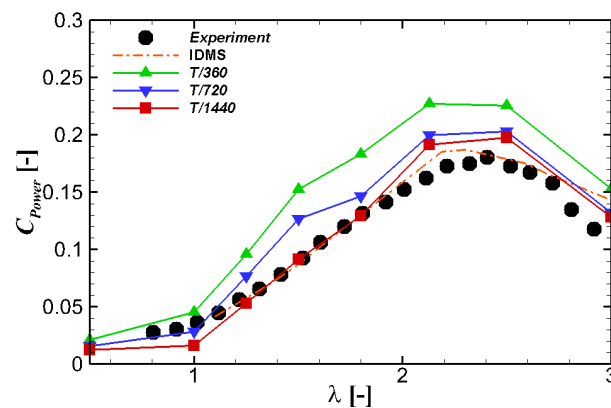

Figure 12. Power curve of the clean turbine predicted using CFD for three different time step sizes in comparison with the experimental data.
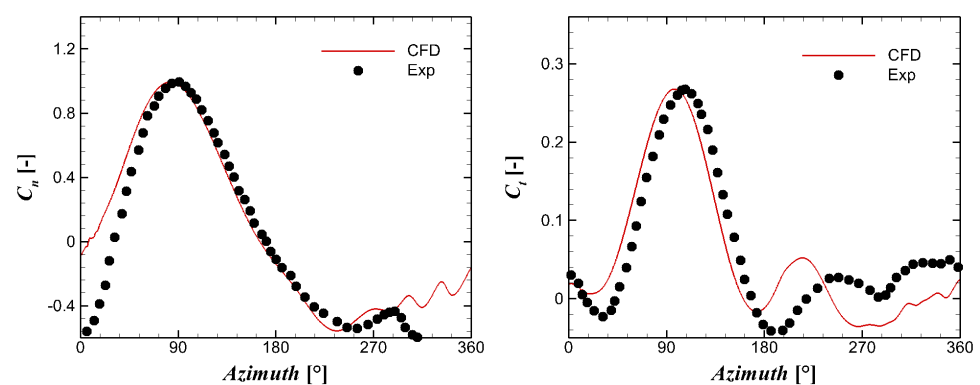

Figure 13. Azimuthal loads predicted using CFD in comparison with the experimental data.

4.4. Performance of VAWT Employed with Gurney Flap

In this section, the performance of the vertical axis wind turbine employed with a Gurney flap is investigated. The integral values and the azimuthal variation of the loads are investigated in detail to improve the understanding of VAWT aerodynamics equipped with Gurney flaps. The cases considered are listed in Table 4.

Table 4. Test cases for the height effect study for the two-bladed rotating vertical axis wind turbine with NACA-0021 airfoil.

Case Nr.	GF Angle	GF Height
1	90°	0.5%c
2	90°	1%c
3	90°	2%c
4	90°	4%c
5	90°	6%c
6	105°	0.5%c
7	105°	1%c
8	105°	2%c

4.4.1. Gurney Flap Height and Angle Effects

In this section, unsteady loads over the azimuth angle in the normal and tangential directions are analyzed. Two Gurney flap angles for three different flap heights are considered for the studies. In addition to that, for each case, the flow field at a selected azimuth position is compared to illustrate the source of the load characteristics.

Figures 14a,b show the normal and tangential force coefficients acting on the turbine blade for the Gurney flap configuration of 0.5%c at two flap angles 90° and 105°. The considered tip speed ratio is $\lambda = 2.13$. This is where the turbine is near the optimal position for the baseline case. It can be seen that the normal and tangential force coefficients increase starting from the azimuth angle of $\theta = 0°$ until the azimuth angle of $\theta = 90°$. These forces then decrease steadily, reaching zero at about $\theta = 180°$. The normal force then becomes negative as the angle of attack is also negative within the downwind region. A different characteristic is observed for the tangential force. It is shown that, for an azimuth angle larger than 180°, the tangential force in general remains constant around the zero level. This shows that the (negative) lift generated within the downwind phase has only a small contribution to the tangential force component.

Another thing to notice while looking at the azimuthal load curves is that a strong unsteady behavior is shown near the maximum level of aerodynamic loads, which indicates the starts of the stall phase. This effect is more prominent for normal loads than the tangential loads. One can see clearly that the Gurney flap angle of 90° presents stronger fluctuations than the angle of 105°, although at the same time, it generates greater normal and tangential forces. This is consistent with the investigations carried out for the static airfoil case in Section 3, where the Gurney flap angle of 90° has a higher lift improvement. To better understand this phenomenon, the crosswise vorticity component is plotted in Figure 15. This is defined as follows:

$$\omega_z = \frac{\partial v}{\partial x} - \frac{\partial u}{\partial y} \tag{11}$$

with u and v being the axial and lateral velocity components. The plot was made for the azimuth angle of 90°, where the fluctuations were already observed. It becomes clear that the flow field in the proximity of the trailing edge for both cases are fairly different. The case with the Gurney flap angle of 90° (Figure 15a,b) presents stronger Karman-street-like vortex oscillations in the wake than for the higher flap angle. This becomes the main source of load oscillations but also creates greater power improvement at the same time.
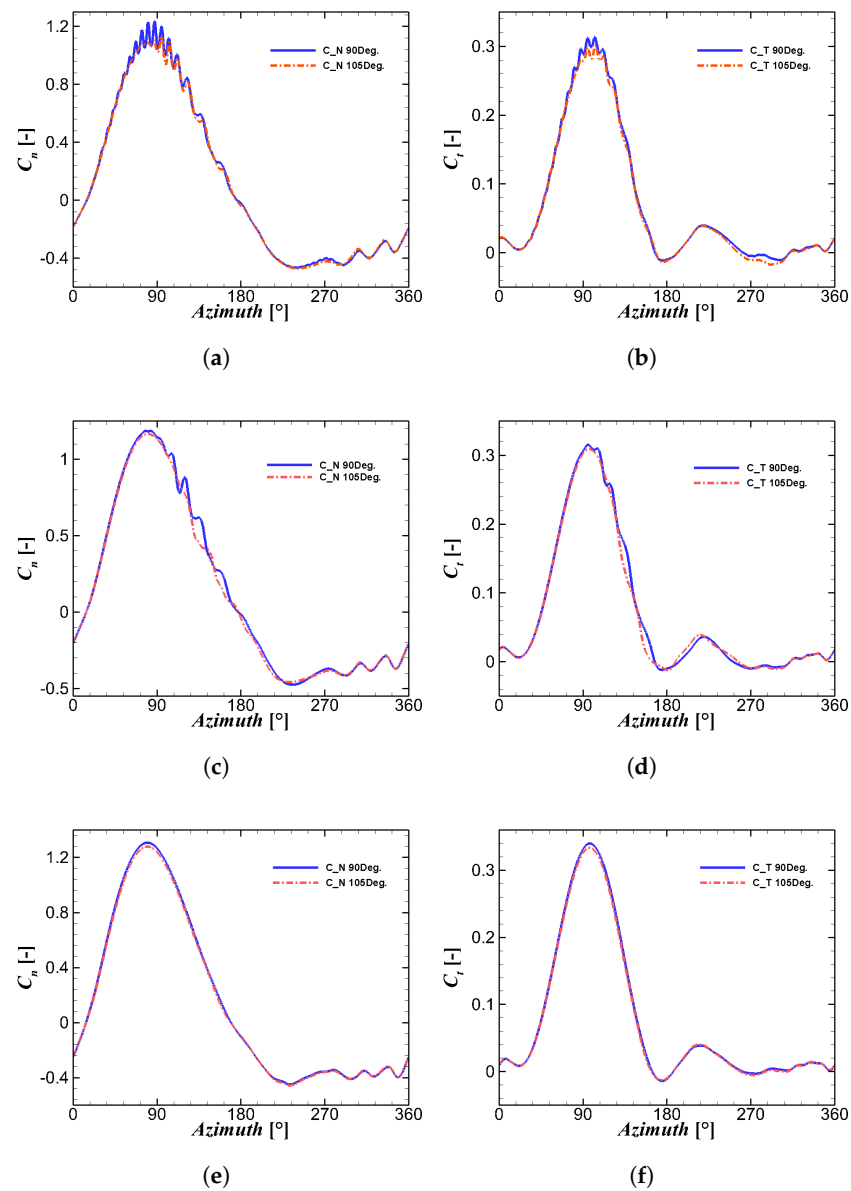
Figure 14. Influence of the Gurney flap angle on the azimuthal normal force (C_n) and tangential force (C_t) coefficients at a tip speed ratio of $\lambda = 2.13$. (**Top**): GF height of 0.5%*c* in (**a**,**b**), (**middle**): GF height of 1%*c* in (**c**,**d**), (**bottom**): GF height of 2%*c* in (**e**,**f**).
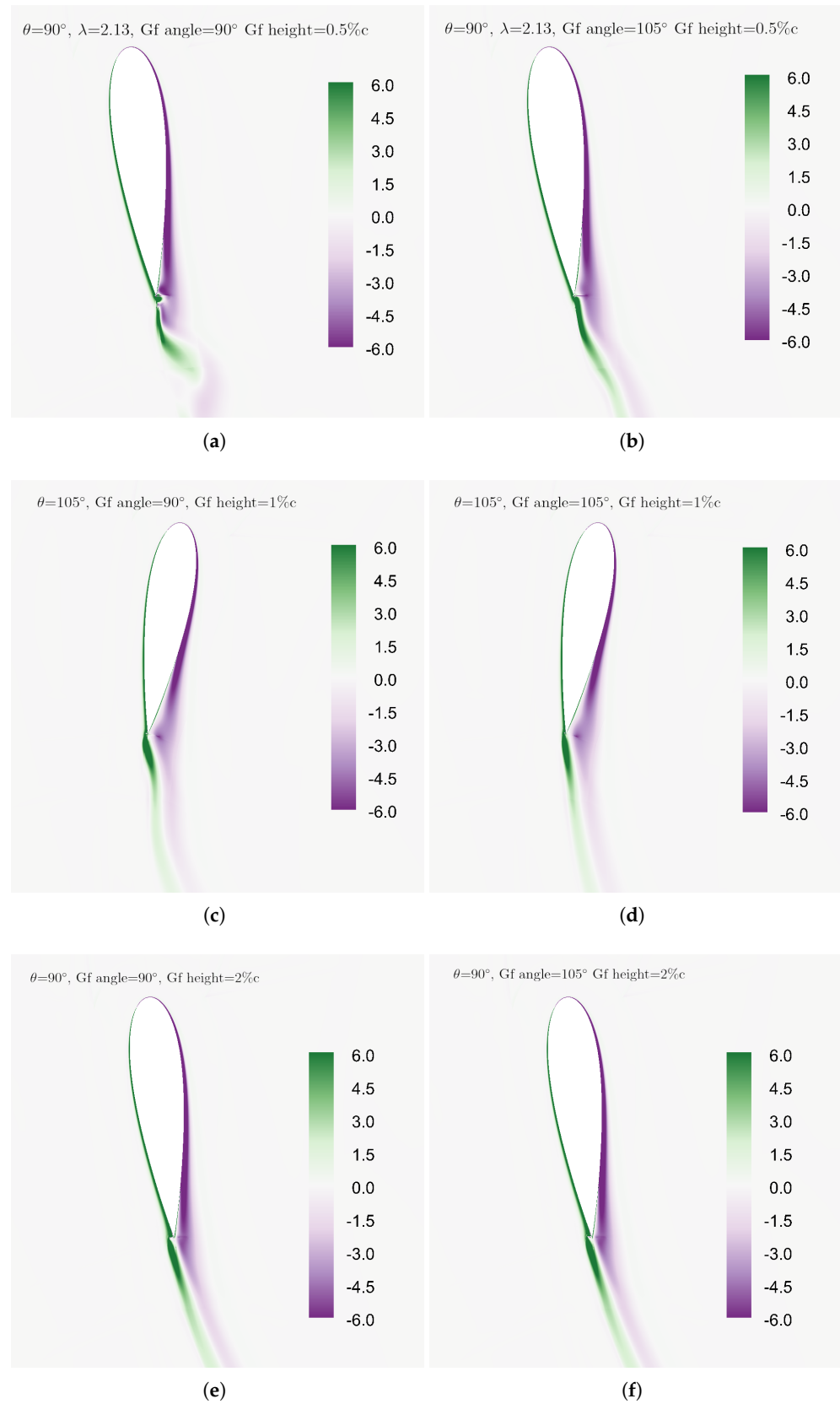
Figure 15. Spanwise vorticity contour at a tip speed ratio of $\lambda = 2.13$. (**Top**): GF height of 0.5%c in (**a**,**b**), (**middle**): GF height of 1%c in (**c**,**d**), (**bottom**): GF height of 2%c in (**e**,**f**).

The results for the Gurney flap height of 1%*c* are presented in Figure 14c,d. Similar to the observations made for the lower Gurney flap height, the azimuthal loads increase starting from the azimuth angle of $\theta = 0°$ to the azimuth angle of $\theta = 90°$. The maximum loads are obtained at an azimuthal angle of 90°. A light unsteady behavior is also shown near the maximum load position, which indicates the stall region up to an azimuthal angle of $\theta = 110°$. However, it is clearly shown that, now, the fluctuations are much weaker than the shorter flap height. This is also indicated clearly in the vorticity field in Figure 15c,d.

By increasing the flap height further to 2%*c*, one can see that the fluctuations are now suppressed completely within the upwind part of the blade rotation, as demonstrated in Figure 14e,f. No huge differences are noticed between the two flap angles (90° and 105°), but a slightly better result is shown for the flap angle of 90°.

In Figure 16, the enlarged view of the total velocity in rotating frame of reference near the trailing edge area is plotted. It can be seen that the velocity field on the pressure side of the airfoil changes with increasing GF height for two different GF angles. In Figure 16a,b, it can be seen that the 90° flap angle generates substantial velocity recovery just downstream of the flap. This induces unsteadiness, which is represented by load fluctuations. This effect becomes weaker as the flap angle is increased to 105°. With increasing flap height, the local velocity recovery is no longer observed. Interestingly, now, the velocity deficit upstream of the flap increases in size. This changes the direction of the blade wake centerline and improves the rotor performance.
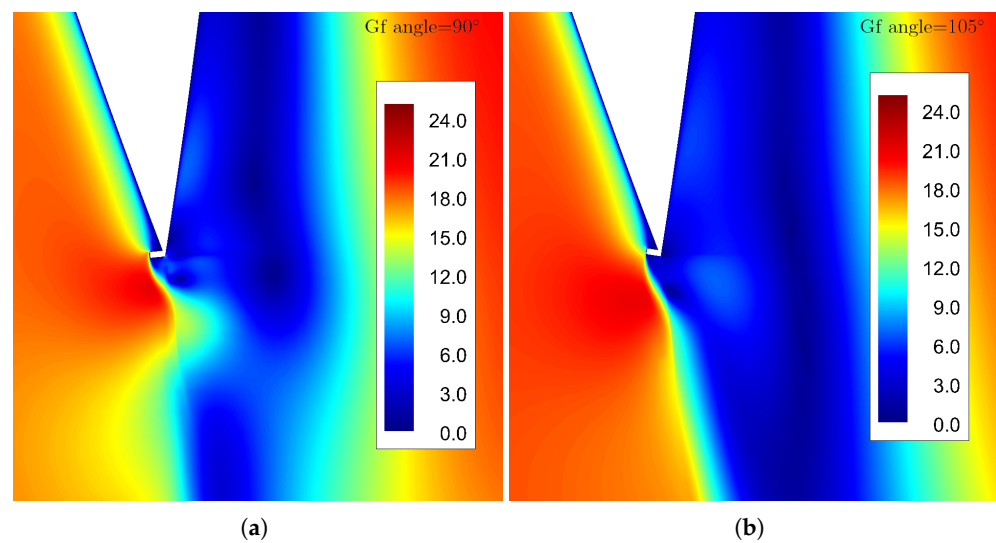

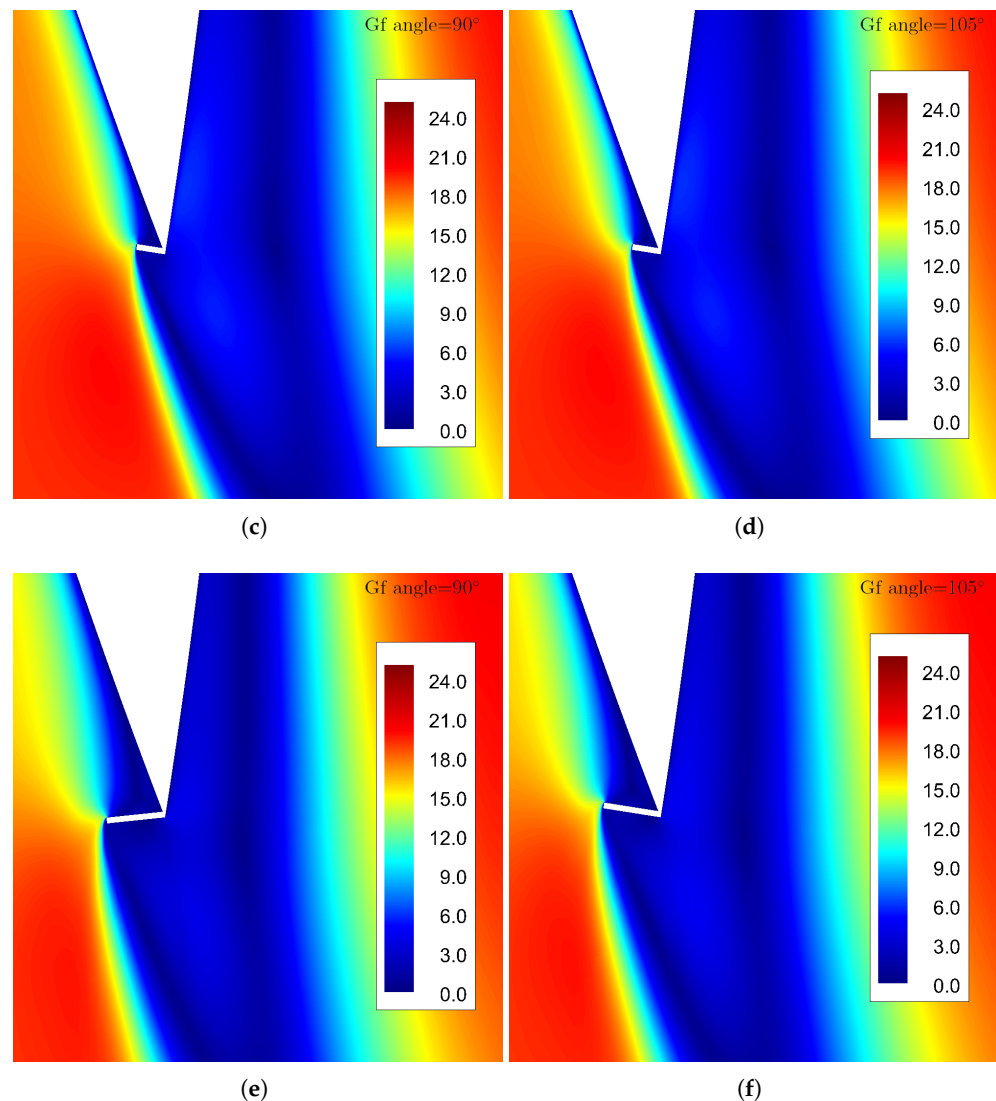(**a**)   (**b**)

Figure 16. *Cont.*

Figure 16. Total velocity plot (in m/s) in the rotating frame of reference at a tip speed ratio of $\lambda = 2.13$. (**Top**): GF height of 0.5%c in (**a**,**b**), (**middle**): GF height of 1%c in (**c**,**d**), (**bottom**): GF height of 2%c in (**e**,**f**).

4.4.2. Rotor Power and Optimal Operation

Having investigated the Gurney flap height and angle effects in the previous section, it can be inferred that the load fluctuations decrease with increasing flap angle at a small value of the flap height. However, this is also followed by a reduction in maximum tangential force. By increasing the flap height, the fluctuations are suppressed and, at the same time, the difference between the flap angle of 90° and 105° becomes insignificant. To further analyze the loads and to give a better suggestion for future development of VAWT designs, two additional simulations were performed for the flap angle of 90° for the flap heights of 4%c and 6%c. The results are presented in Figure 17.

Now, it can be clearly seen that both the normal and tangential load components increase with increasing flap height. Interestingly, the load fluctuations are suppressed as well. Figure 17 shows that the fluctuations take place only for the flap heights of 0.5%c and 1%c. This shows that it is beneficial to use longer flap than the shorter flap version in contrast to the observations made for the static airfoil case in Section 3 especially for a large solidity turbine such as the one considered in the present work.
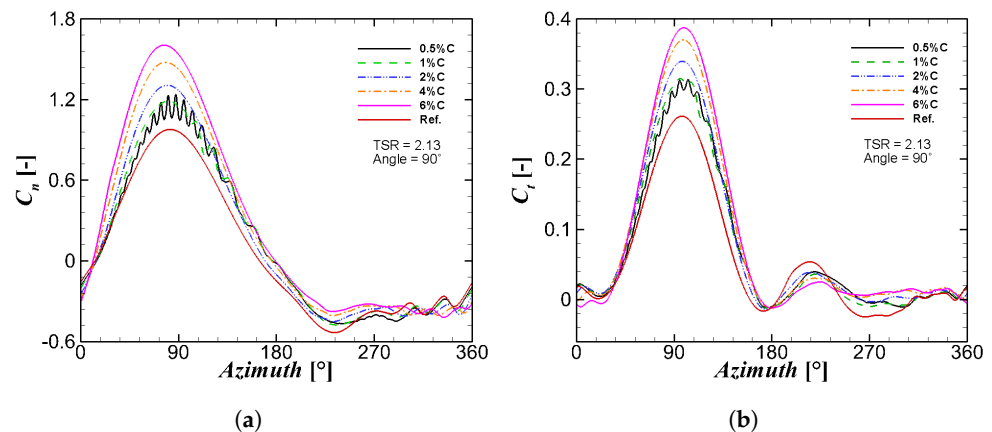
Figure 17. Variation in the normal C_n and tangetial C_t force coefficients for five different GF heights: 0.5%c, 1%c, 2%c, 4%c, and 6%c in comparison with the clean turbine case. (**a**) Normal component and (**b**) tangential component.

Figure 18 presents the impact of the Gurney flap height on the power production of the VAWT for different tip speed ratios. A larger power coefficient indicates larger output torque. The tip speed ratio ranges from $\lambda = 0.5$ to $\lambda = 3.0$. Five different Gurney flaps were investigated, namely 0.5%c, 1%c, 2%c, 4%c, and 6%c, and compared to the baseline case. The first thing one notices is that mounting a Gurney flap at the trailing edge of the blade increases the power production of the VAWT remarkably for tip speed ratios between $0.5 < \lambda < 2.5$. As it can be seen from Figure 18 that, for low tip speed ratios $(0.5 < \lambda < 1.5)$, the relative growth rate of the power coefficient while varying the Gurney flap heights is relatively low, although the power is still much higher than the baseline case. This aspect solves an important operation problem of self-starting. For $(0.5 < \lambda < 1.0)$, the best performance is obtained for a GF height of $h = 1\%c$ and the minimum is obtained at a GF height $h = 2\%c$. Near the optimal operating regime at $\lambda = 2.13$, further increasing the GF height notably increases the power coefficient of the VAWT to more than 0.3. The optimal value is obtained for tip speed ratio $\lambda = 2.19$ for Gurney flap height $h = 6\%c$. At high tip speed ratios, the discrepancy in the power production is again very small and the lowest power coefficient C_{Power} is obtained for a GF height of $h = 6\%c$. At this location, the minimum drag force will be dominant for obtaining higher power; thus, usage of a long Gurney flap is not desirable.
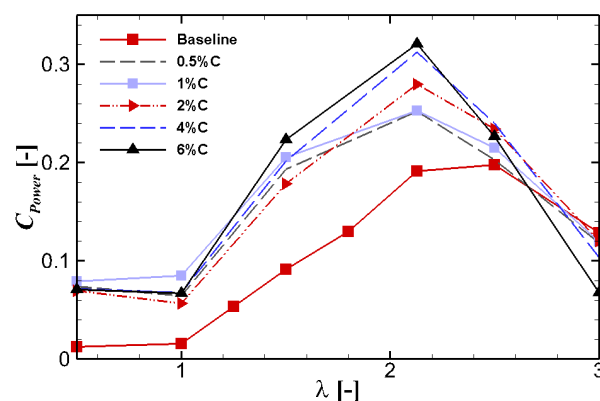

Figure 18. Power curve for five different GF heights: 0.5%c, 1%c, 2%c, 4%c, and 6%c in comparison with the clean turbine case.

As described for some selected cases in Section 4.4.1 and in Figure 17, the usage of Gurney flaps changes the load characteristics of the blades and, consequently, the rotor

performance shown in Figure 18. It becomes evident from Figure 16 that the Gurney flap changes the direction of the wake centerline. This artificially creates an additional camber effect in the fluid flow, which in turn enhances the lift force acting on the rotor blade. This is identified as the main source of performance improvement. However, in contrast with the low solidity rotors considered in past studies, the performance of high solidity rotor is less affected by the drag increase due to Gurney flaps. This allows blade designers to use longer Gurney flaps in their designs. Furthermore, this aspect also modifies the unsteady characteristic of the flow field commonly denoted as dynamic stall. The effect seems to be influenced by the flap and could potentially be controlled. Future studies in this direction are strongly encouraged.

5. Conclusions

The present paper delivers a computational study on the flow characteristics of static airfoil and rotating vertical axis wind turbine equipped with Gurney flaps in order to provide quantitative and qualitative data on the aerodynamic performance of this device. The following conclusions can be drawn:

- Increasing the Gurney flap height results in increased lift and drag coefficients for the static airfoil case. However, a height of $0.5\%c$ generates a very small increase in drag and provides the highest lift-to-drag ratio compared to the clean airfoil.
- The lift improvement is greater for the 90° configuration than the 105° configuration.
- For the rotating VAWT case, the load fluctuations decrease with increasing flap angle at a small value of the flap height. By increasing the flap height, the fluctuations are suppressed and, at the same time, the difference between the flap angles 90° and 105° becomes insignificant. This shows that it is beneficial to use the longer flap than the shorter flap version in contrast to the observations made for the static airfoil case, especially for large solidity turbines.
- Mounting a Gurney flap at the trailing edge of the blade increases the power production of the VAWT remarkably for tip speed ratios between $0.5 < \lambda < 2.5$.
- At very low tip speed ratios, the best performance is obtained for the Gurney flap height of $h = 1\%c$.
- Within the operating range of the turbine at $1 \le \lambda \le 2.5$, further increasing the Gurney flap height increases the power coefficient of the VAWT notably to more than 0.3. The optimal value is obtained for tip speed ratio $\lambda = 2.13$ for Gurney flap height $h = 6\%c$.
- At large tip speed ratios, the usage of a Gurney flap is not beneficial.
- The present work extends the existing literature on VAWTs with Gurney flaps especially for a two-bladed rotor having high solidity. The results show that, for this type of turbine, the Gurney flap height can be increased to a larger value, extending the limit of around 2% for the lower solidity turbine.

Author Contributions: Y.C.: data curation, draft writing, and analyses. G.B.: conceptualization, supervision, data curation, draft writing, and analyses. All authors have read and agreed to the published version of the manuscript.

Nomenclature

c	blade chord, (m)
C_L	lift coefficient, $(-)$
C_D	drag coefficient, $(-)$
C_{Power}	power coefficient, $(-)$
F_t	sectional tangential force, (N/m)
F_n	sectional normal force, (N/m)
N	number of blade, $(-)$
R	radius of turbine, (m)
$P_{Turbine}$	rotor power, (Watt)
U_∞	free stream wind velocity in axial direction, (m/s)
x, y	Cartesian coordinate, (m)
u, v	axial and lateral velocity components, (m/s)
α	angle of attack, (°)
α_p	pitch angle, (°)
Ω	rotational speed, (rad/s)]
ω	vorticity, (1/s)
λ	tip speed ratio, $(-)$
σ	rotor solidity, $(-)$

References

1. Dincer, I. Environmental impacts of energy. *Energy Policy* **1999**, *27*, 845–854. [CrossRef]
2. Bangga, G.; Lutz, T.; Dessoky, A.; Krämer, E. Unsteady Navier-Stokes studies on loads, wake, and dynamic stall characteristics of a two-bladed vertical axis wind turbine. *J. Renew. Sustain. Energy* **2017**, *9*, 053303. [CrossRef]
3. Bangga, G.; Hutomo, G.; Wiranegara, R.; Sasongko, H. Numerical study on a single bladed vertical axis wind turbine under dynamic stall. *J. Mech. Sci. Technol.* **2017**, *31*, 261–267. [CrossRef]
4. Ferreira, C.S.; Bijl, H.; Van Bussel, G.; Van Kuik, G. Simulating dynamic stall in a 2D VAWT: Modeling strategy, verification and validation with particle image velocimetry data. *J. Physics Conf. Ser.* **2007**, *75*, 012023. [CrossRef]
5. Carr, L.W. Progress in analysis and prediction of dynamic stall. *J. Aircr.* **1988**, *25*, 6–17. [CrossRef]
6. McCroskey, W.J. *The Phenomenon of Dynamic Stall*; Technical Report; National Aeronuatics and Space Administration Moffett Field Ca Ames Research Center: Mountain View, CA, USA, 1981.
7. Mercado-Colmenero, J.M.; Rubio-Paramio, M.A.; Guerrero-Villar, F.; Martin-Doñate, C. A numerical and experimental study of a new Savonius wind rotor adaptation based on product design requirements. *Energy Convers. Manag.* **2018**, *158*, 210–234. [CrossRef]
8. Almohammadi, K.; Ingham, D.; Ma, L.; Pourkashanian, M. Modeling dynamic stall of a straight blade vertical axis wind turbine. *J. Fluids Struct.* **2015**, *57*, 144–158. [CrossRef]
9. Liebeck, R.H. A class of airfoils designed for high lift in incompressible flow. *J. Aircr.* **1973**, *10*, 610–617. [CrossRef]
10. Bao, N.; Ma, H.; Ye, Z. Experimental study of wind turbine blade power augmentation using airfoil flaps, including the Gurney flap. *Wind. Eng.* **2000**, *24*, 25–34. [CrossRef]
11. Zhang, Y.; Ramdoss, V.; Saleem, Z.; Wang, X.; Schepers, G.; Ferreira, C. Effects of root Gurney flaps on the aerodynamic performance of a horizontal axis wind turbine. *Energy* **2019**, *187*, 115955. [CrossRef]
12. Syawitri, T.P.; Yao, Y.F.; Yao, J.; Chandra, B. The effect of gurney flap on flow characteristics of vertical axis wind turbine. *Int. J. Mod. Phys. B* **2020**, *34*, 2040107. [CrossRef]
13. Zhu, H.; Hao, W.; Li, C.; Luo, S.; Liu, Q.; Gao, C. Effect of geometric parameters of Gurney flap on performance enhancement of straight-bladed vertical axis wind turbine. *Renew. Energy* **2021**, *165*, 464–480. [CrossRef]
14. Zhu, H.; Hao, W.; Li, C.; Ding, Q. Numerical study of effect of solidity on vertical axis wind turbine with Gurney flap. *J. Wind. Eng. Ind. Aerodyn.* **2019**, *186*, 17–31. [CrossRef]
15. Yan, Y.; Avital, E.; Williams, J.; Cui, J. Performance improvements for a vertical axis wind turbine by means of Gurney flap. *J. Fluids Eng.* **2020**, *142*. [CrossRef]
16. Kroll, N.; Rossow, C.C.; Becker, K.; Thiele, F. The MEGAFLOW project. *Aerosp. Sci. Technol.* **2000**, *4*, 223–237. [CrossRef]
17. Jameson, A.; Schmidt, W.; Turkel, E. Numerical solution of the Euler equations by finite volume methods using Runge Kutta time stepping schemes. In Proceedings of the 14th Fluid and Plasma Dynamics Conference, Palo Alto, CA, USA, 23–25 June 1981; p. 1259.
18. Benek, J.; Steger, J.; Dougherty, F.C. A flexible grid embedding technique with application to the Euler equations. In Proceedings of the 6th Computational Fluid Dynamics Conference Danvers, Danvers, MA, USA, 13–15 July 1983; p. 1944.
19. Chan, W.; Gomez, R.; Rogers, S.; Buning, P. Best practices in overset grid generation. In Proceedings of the 32nd AIAA Fluid Dynamics Conference and Exhibit, St. Louis, MI, USA, 24–26 June 2002; p. 3191.

20. Schwarz, T. The Overlapping Grid Technique for the Time Accurate Simulation of Rotorcraft Flows. In Proceedings of the 31st European Rotorcraft Forum, Florence, Italy, 2005; p. 86.

21. Jameson, A. Time dependent calculations using multigrid, with applications to unsteady flows past airfoils and wings. In Proceedings of the 10th Computational Fluid Dynamics Conference, Honolulu, HI, USA, 24–26 June 1991; p. 1596.

22. Radespiel, R.; Rossow, C.; Swanson, R. Efficient cell-vertex multigrid scheme for the three-dimensional Navier-Stokes equations. *AIAA J.* **1990**, *28*, 1464–1472. [CrossRef]

23. Menter, F.R. Two-equation eddy-viscosity turbulence models for engineering applications. *AIAA J.* **1994**, *32*, 1598–1605. [CrossRef]

24. Celik, I.; Karatekin, O. Numerical experiments on application of Richardson extrapolation with nonuniform grids. *J. Fluids Eng.* **1997**, *119*, 584–590. [CrossRef]

25. Bangga, G.S.; Lutz, T.; Krämer, E. An Examination of Rotational Effects on Large Wind Turbine Blades. In Proceedings of the 11th EAWE PhD Seminar on Wind Energy in Europe, Stuttgart, Germany, 23–25 September 2015.

26. Bangga, G.; Solichin, M.; Daman, A.; Sa'adiyah, D.; Dessoky, A.; Lutz, T. Aerodynamic performance of a small vertical axis wind turbine using an overset grid method. In *AIP Conference Proceedings*; AIP Publishing LLC: Melville, NY, USA, 2017; Volume 1867, p. 020005.

27. Bangga, G. Numerical studies on dynamic stall characteristics of a wind turbine airfoil. *J. Mech. Sci. Technol.* **2019**, *33*, 1257–1262. [CrossRef]

28. Storms, B.L.; Jang, C.S. Lift enhancement of an airfoil using a Gurney flap and vortex generators. *J. Aircr.* **1994**, *31*, 542–547. [CrossRef]

29. Jang, C.; Ross, J.; Cummings, R. Computational evaluation of an airfoil with a Gurney flap. In Proceedings of the 10th Applied Aerodynamics Conference, Palo Alto, CA, USA, 22–24 June 1992.

30. Maughmer, M.D.; Bramesfeld, G. Experimental investigation of Gurney flaps. *J. Aircr.* **2008**, *45*, 2062–2067. [CrossRef]

31. Zanotti, A.; Gibertini, G. Experimental investigation of the dynamic stall phenomenon on a NACA 23012 oscillating airfoil. *Proc. Inst. Mech. Eng. Part G J. Aerosp. Eng.* **2013**, *227*, 1375–1388. [CrossRef]

32. Maeda, T.; Kamada, Y.; Murata, J.; Yamamoto, M.; Ogasawara, T.; Shimizu, K.; Kogaki, T. Study on power performance for straight-bladed vertical axis wind turbine by field and wind tunnel test. *Renew. Energy* **2016**, *90*, 291–300.

33. Bangga, G.; Dessoky, A.; Lutz, T.; Krämer, E. Improved double-multiple-streamtube approach for H-Darrieus vertical axis wind turbine computations. *Energy* **2019**, *182*, 673–688. [CrossRef]